Research in Astronomy and Astrophysics, 25:055013 (10pp), 2025 May

https://doi.org/10.1088/1674-4527/adcc7d
CSTR: 32081.14.RAA.adcc7d

Photometric Calibration of Spectral Imaging CoronaGraph with Dual-wavelength Observation

Ning Tang[1], Wei-Xin Liu[1], Xian-Liang Mao[1], Xiao-Yu Yu[1], Xiu-Hui Zuo[1], Bo-Yu Sun[1], Hao-Ran Zheng[1], Da-Yang Liu[1], Xue-Fei Zhang[2], Ming-Zhe Sun[1], Zheng-Hua Huang[1], Hui Fu[1], and Li-Dong Xia[1]
[1] Shandong Key Laboratory of Optical Astronomy and Solar-Terrestrial Environment, Institute of Space Sciences, Shandong University, Weihai 264209, China; liuwx@sdu.edu.cn
[2] Yunnan Observatories, Chinese Academy of Sciences, Kunming 650011, China
Received 2025 February 13; revised 2025 March 29; accepted 2025 April 8; published 2025 May 20

Abstract

The Spectral Imaging CoronaGraph (SICG) serves as the optical observation equipment of E-corona in the Chinese Meridian Project Phase II, which aims at monitoring the initial source of solar activities. For the purpose of in-depth exploration and space weather forecast in the full chain of Sun–Earth space, SICG is designed to work at two wavelengths of 637.4 and 530.3 nm in the quasi-simultaneous observation mode. Thus, the photometric calibration is more challenging to guarantee accurate scientific data of SICG. Two solar photometers are specially developed to match the observing wavelengths and make the photoelectronic conversion traceable. Correspondingly, the calibration process selects the solar disk center as the brightness reference, which compensates for the photometric losses along the atmospheric transmission path. This study derives the calibration coefficients from the two photometers for the E-coronal brightness processing in real time. By modeling aerosol absorption and scattering and comparing with continuous flat-field observation, the photometric calibration of SICG is evaluated with deviations of 2.1% and 2.3% at 637.4 nm and 530.3 nm, respectively. Based on this, the evolution speed of a multi-temperature coronal loop was analyzed, facilitating further research into the physical mechanisms of coronal mass ejections.

Key words: Sun: corona – instrumentation: miscellaneous – methods: data analysis – techniques: photometric

1. Introduction

The solar corona is a million-degree plasma that acts as a site for eruptive activity and the source of the solar wind (Aschwanden & Nitta 2000; Judge et al. 2019). Investigating the corona is essential for space physics, particularly in predicting hazardous space weather (Zaki et al. 2016). Compared to the photosphere, the brightness of the corona in the visible spectrum is extremely faint, much lower than 10^{-6}, and decreases rapidly with radial distance. Now that the corona is hidden by the shiny solar disk, it can only be observed during total solar eclipses or with the help of coronagraphs. A coronagraph is a telescope equipped with an occulting disk that blocks the light from the photosphere, allowing direct observation of the corona (de Wijn et al. 2012).

Both space-based and ground-based coronagraphs have been developed to gain scientific data for exploring coronal mass ejections (CMEs) and solar wind (Kohl et al. 2008; Fineschi et al. 2012). With no disturbance from atmospheric scattering light, the former has advantages in coronal observation in the larger field of view (FOV), such as coronagraphs onboard SOHO, STEREO, and the PSP (Newmark et al. 2007; Howard et al. 2008; Kaiser et al. 2008; Raouafi et al. 2023). However, the ground-based coronagraphs are subject to additional limitations from atmospheric distortions and local observing conditions, which significantly affect the observation FOV and spectral line (Marois et al. 2006; Xin et al. 2020; Ltaief et al. 2021; Sha et al. 2023), such as UCoMP, K-Cor, and YOGIS coronagraphs. In 2023, a new coronagraph, the Spectral Imaging CoronaGraph (SICG), was established at the same site as YOGIS (at Yulong Observatory in Lijiang City, Yunnan Province, China) with the support of Chinese Meridian Project Phase II (Wang et al. 2020). SICG is designed to observe E-coronal emission lines at 637.4 and 530.3 nm, which monitor the material transport and magnetic field link in the chain of Sun–Earth space (Liu et al. 2025).

Besides the coronal structure and spectral characteristics, its brightness is another important parameter for analyzing the mass and density of CMEs (Zhang et al. 2022). So, the photometric calibration is essential during the testing and operation stages of coronagraphs. As for the space-based coronagraph, a calibration device, for instance, the Solar Corona Optical Test Chamber (Brueckner et al. 1995) is employed prior to launch; while some standard stars within the FOV or a calibration lamp are adopted during the on-orbit mission (Morrill et al. 2006; Colaninno & Howard 2015). As for the ground-based coronagraph, an inevitable issue is that

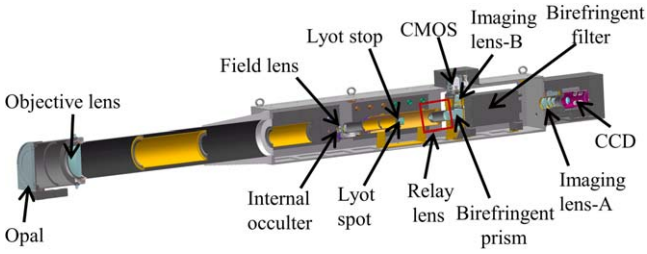

Figure 1. Optical and mechanical design of the SICG.

the real-time atmospheric transmittance should be determined to ensure accurate measurement of coronal brightness. One solution is to estimate the atmospheric transmittance with a verified model such as the LOWTRAN algorithm, which, however, has poor accuracy in coronagraph calibration due to the deviation between actual atmospheric conditions and standard models (Ouyang et al. 1981). Another solution is to use a photometer of the same wavelength to monitor solar disk brightness for atmospheric transmittance calculation and coronal radiance compensation (Minarovjech et al. 2003).

To provide reliable scientific data for research and space weather forecasting, the SICG presents more challenging requirements for photometric calibration due to the fact that the coronagraph operates in the dual-wavelength mode and has a narrow bandwidth of 0.1 nm at each wavelength. This paper deeply analyzes the calibration requirements and proposes a simultaneous monitoring method of atmospheric transmittance at both wavelengths. With the help of two matching solar photometers and full-disk imaging, the brightness of E-corona can be traced back to the solar photosphere center irradiance under a well-designed calibration process. Then, the atmospheric transmittance modeling and flat-field intensity are compared with photometer data to evaluate the calibration uncertainty. In view of this, the high-quality scientific data of SICG have potential in studying the temporal evolution of coronal loops and the physical mechanisms of CMEs, particularly when combined with the space-based coronagraphs for joint observation.

2. SICG Photometric Calibration Principles

2.1. System Design of SICG

The SICG, located at the Yulong Observatory in Lijiang, is designed for observing the inner corona with an FOV ranging from $1.05R_{\odot}$ to $2.0R_{\odot}$ (solar radii). As shown in Figure 1, light from the photosphere entering the SICG is focused by the objective lens and blocked by the internal occulter, while the coronal light passes through the following optical lens group for imaging. To sense the quite weak coronal light, a specially designed Lyot stop and Lyot spot are adopted to deal with the diffracted light from the objective lens edge and the ghost image generated by multiple reflections of lens surface. Meanwhile, the optical path divides into two branches with a birefringent prism. The reflected beam is directed to image the objective lens for dust monitoring, and the transmitted beam passes through a tunable birefringent filter to select the E-coronal emission line at either 637.4 nm or 530.3 nm for observation. Then the CCD sensor (Andor iKon-L 936) captures the raw coronal images at several frequency points to obtain peak-intensity maps, coronal Dopplergrams, line width maps, and so on. Finally, the main observational specifications of SICG are as follows: a time resolution of 30 s (with observations at five frequency points), an observation frequency bandwidth of $\leqslant$1.2 Å, spectral line width measurement accuracy of $\pm$0.15 Å, and velocity measurement accuracy of $\pm 3\,\mathrm{km\,s^{-1}}$ (Tomczyk et al. 2008; Morton et al. 2016).

2.2. Two Photometers Equipped with SICG

As mentioned in Tang et al. (2023), the detected light intensity of the SICG imaging sensor would be affected by two main factors. One comes from the total transmissivity of the optical system, including the lens, prism, and filters. The other is owing to the distance changing from Earth to Sun following the revolution, and the atmospheric transmittance varying with the Earth's rotation. The former is constant, and the latter is continuously altering during SICG observation. For accurate data, the photometric response of SICG should be calibrated to a certain standard. One feasible solution is to choose the center of the solar disk as the irradiance reference. By recording both the solar photosphere and coronal images, the actual brightness can be expressed by the ratio to the disk center. However, the coronagraph blocks the solar disk during observation, and its irradiance cannot be monitored in real time. Thus, two photometers, compensating for the corona photometric alteration with Earth's revolution and rotation, are equipped and aligned with the SICG, as highlighted in Figure 2. Photometers A and B operate at two observation wavelengths of 637.4 and 530.3 nm separately, which receive light from the solar disk with a single photodetector. The optical systems of both photometers are identically designed, as shown in Figure 3.

A filter selects light from the solar disk before it is focused by a lens onto a photodetector, while the diaphragms are combined to suppress stray light, and the aperture limits the FOV. Both photometers utilize NIST-calibrated photodetectors S142C to convert solar disk flux into watts (W). Each photodetector contains an integrating sphere photodiode and has a linearity of measurement of $\pm$0.5%. Before observation, the photometers have also been tested and calibrated considering the optical elements, and the photoelectric signal is acquired by an on-site conversion module.

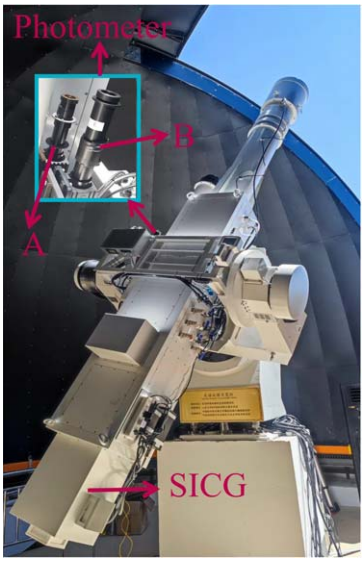

Figure 2. SICG installed at Yulong Observatory in Lijiang with photometers A and B as illustrated in the blue box.

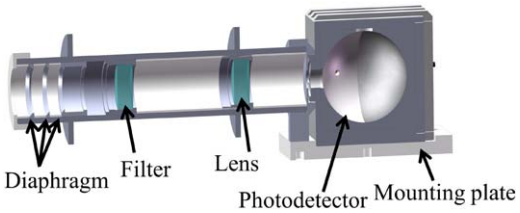

Figure 3. Internal structure of the photometer.

2.3. Calibration Data Processing Workflow

According to the SICG and photometer design, the photometric calibration workflow could be adopted as illustrated in Figure 4. There are two processing sections before normal observation. In the solar disk observation mode, the internal occulter is removed, and the entrance window of SICG is covered with a Baader AstroSolar filter (OD 3.8) to attenuate the strong light of the photosphere. As given in Figure 5(a), the solar disk is imaged by the optical system to provide the solar disk center intensity as the reference value. By applying the Baader AstroSolar filter attenuation factor, the actual pixel value at the solar disk center is derived within a certain exposure time. Meanwhile, the solar irradiance surveyed by the photometers is recorded with $R_{sp}(\lambda, t_0)$ for further coronal photometric calibration coefficient (k_0) calculation. In the coronal observation mode, the internal occulter is reinstalled and SICG captures several images at different frequency points within a wavelength. In fact, the sky background and F-corona must also be further removed by subtracting the corona raw images from the background image, as the observation frequency points are set at 637.4 and 530.3 nm. The E-corona flux recorded in DN (digital number)

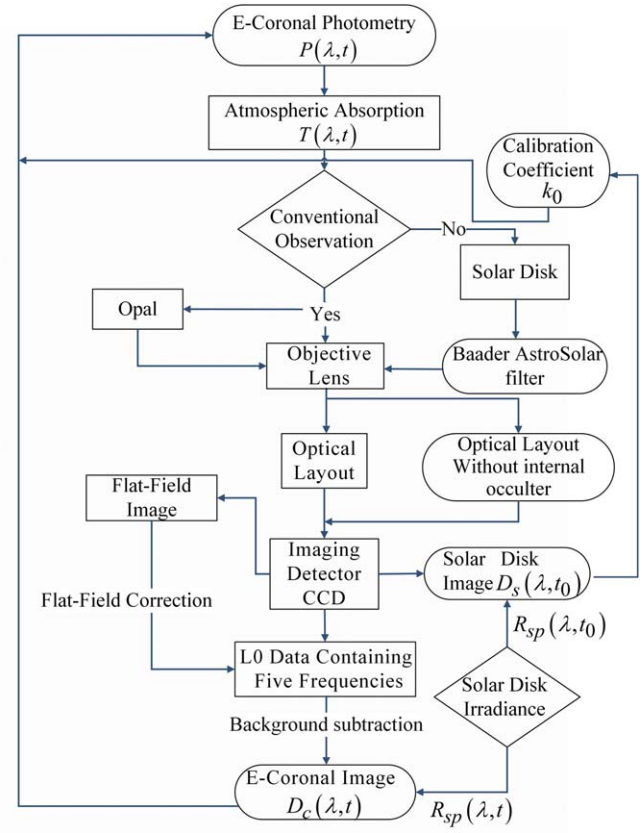

Figure 4. Processing workflow for the photometric calibration of SICG data.

is given in Figure 5(b). To combine the data of the solar disk and corona, the flat-field calibration is noteworthy to be executed (Sivaramakrishnan & Oppenheimer 2006; Casini et al. 2021). During solar disk observation, the opal in front of the objective lens is covered to obtain the flat-field image as given in Figure 5(c).

The recorded intensity in the central region is higher compared with that in the observation region from $1.05R_{\odot}$ to $2R_{\odot}$, which indicates an issue of transmission inconsistency primarily caused by the optical system. Then, each pixel DN value could be normalized to the image center point, where it is matched with the solar disk center. Combining with Figures 5(a)–(c), the final coronal image data corrected to the relative brightness of the solar disk center (in units of MSB), is achieved as illustrated in Figure 5(d), which could produce the calibration coefficients following the processing flow of Figure 4.

Additionally, owing to the extreme weakness of the E-coronal data compared to the solar intensity, it is necessary to eliminate the effects of the dark field of the CCD imager in those calibration processes. Before observation, the image with the absence of light with the coronagraph being covered is recorded, which corresponds to the CCD dark current within a certain exposure time. Then, in E-corona data acquisition and

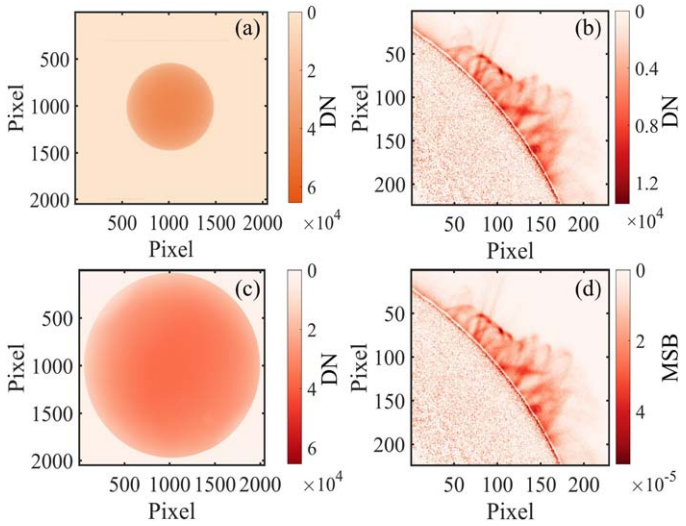

Figure 5. (a) Solar disk observation data covering the Baader AstroSolar filter; (b) DN value image of E-corona within the exposure time; (c) Flat-field observation data without internal occulter; (d) E-corona brightness effective data normalized to unit exposure time.

flat-field correction, the dark field is compensated for an accurate optical signal.

After calibration, the coronagraph turns to normal observation while the solar flux is recorded by the photometer in real time as the Sun orbits in one day. Combining the obtained coronal raw data, the photometer continuous data $R_{sp}(\lambda, t)$, and the flat-field calibration coefficients, the E-coronal images with brightness normalized to the solar disk center $P(\lambda, t)$ can be generated based on the following computing process.

2.4. Photometric Algorithm Tracing Back to Solar Disk Center

Under the condition that the atmospheric absorption effects are identical for light of the same wavelength from both the corona and the solar disk along the same transmission path, the ratio of coronal to solar disk brightness at the upper atmosphere satisfies

$$\frac{R_{c0}(\lambda, t)}{R_{s0}(\lambda, t)} = \frac{\frac{R_c(\lambda,t)}{T(\lambda,t)}}{\frac{R_s(\lambda,t)}{T(\lambda,t)}} = \frac{R_c(\lambda, t)}{R_s(\lambda, t)} \tag{1}$$

where $R_{c0}(\lambda, t)$ and $R_{s0}(\lambda, t)$ represent the radiance values of the corona and solar disk at the upper atmosphere, while $R_c(\lambda, t)$ and $R_s(\lambda, t)$ indicate the irradiance values of the corona and solar disk received on the ground, respectively. The parameter $T(\lambda, t)$ describes the atmospheric absorption effects, i.e., the transmittance along the atmospheric transmission path. By simplifying Equation (1), the same ratio of $R_{c0}(\lambda, t)$ to $R_{s0}(\lambda, t)$ and that of $R_c(\lambda, t)$ to $R_s(\lambda, t)$ can be obtained. This indicates that the impact of atmospheric absorption can be eliminated by simultaneously recording the corona and solar disk irradiance values at the same wavelength. Since the photoelectric conversion of CCD is linear in SICG observation, the irradiance ratio is equivalent to that of the counts of the corona and solar disk images. Thereby, the ratio can be given with

$$\frac{R_{c0}(\lambda, t)}{R_{s0}(\lambda, t)} = \frac{D_c(\lambda, t)}{D_s(\lambda, t)} \cdot \frac{\tau_s(t)}{\tau_c(t)}, \tag{2}$$

where $D_c(\lambda, t)$ and $D_s(\lambda, t)$ represent the count values of the coronal image and solar disk image observed at moment t, respectively. These count values are related to the exposure times $\tau_c(t)$ of the coronal image and $\tau_s(t)$ of the solar disk image. The exposure times are determined by both the atmospheric transmission conditions and fixed instrumental settings of SICG. By normalizing the exposure times, consistency in units is ensured, allowing for a direct comparison of the coronal and solar disk brightness. According to the calibration and observation mode of SICG, the solar disk image recorded by the coronagraph and the solar disk irradiance measured by the photometer are considered equivalent. Thus the solar disk counts $D_s(\lambda, t_0)$ at the initial moment t_0 and $D_s(\lambda, t)$ at the moment t satisfy

$$\frac{D_s(\lambda, t_0)}{D_s(\lambda, t)} \cdot \frac{\tau_s(t)}{\tau_s(t_0)} = \frac{R_{sp}(\lambda, t_0)}{R_{sp}(\lambda, t)}, \tag{3}$$

where $R_{sp}(\lambda, t_0)$ and $R_{sp}(\lambda, t)$ are the corresponding solar disk irradiance values recorded by the photometer at the same moment. By simplifying Equation (3), it can be deduced that

$$D_s(\lambda, t) = \frac{D_s(\lambda, t_0)}{R_{sp}(\lambda, t_0)} \cdot \frac{\tau_s(t)}{\tau_s(t_0)} \cdot R_{sp}(\lambda, t). \tag{4}$$

Then combining Equation (2) and Equation (4), there is

$$\frac{R_{c0}(\lambda, t)}{R_{s0}(\lambda, t)} = \frac{D_c(\lambda, t)}{D_s(\lambda, t_0)} \cdot \frac{R_{sp}(\lambda, t_0)}{R_{sp}(\lambda, t)} \cdot \frac{\tau_s(t_0)}{\tau_c(t)}. \tag{5}$$

Defining the photometric calibration coefficient $k_0 = \frac{R_{sp}(\lambda, t_0)}{D_s(\lambda, t_0)} \cdot \tau_s(t_0)$, we can derive the coronal brightness relative to

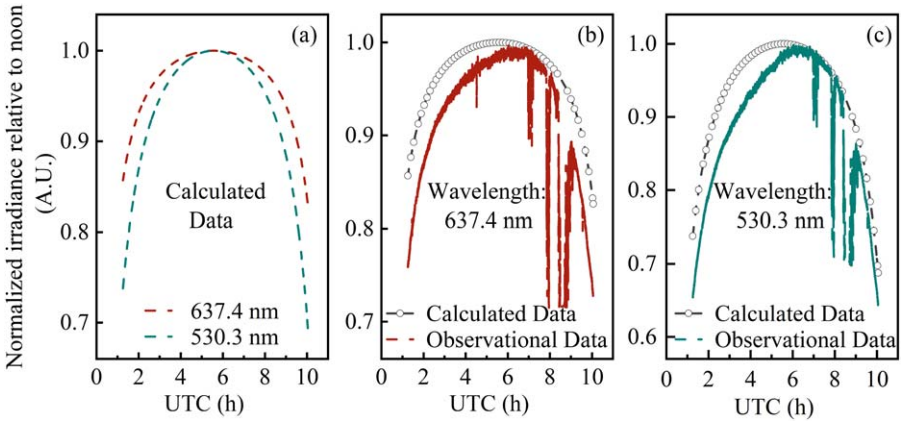

Figure 6. (a) The calculated normalized irradiance relative to noon at 637.4 nm and 530.3 nm on 2024 February 13; (b) Photometer A at 637.4 nm normalized to noon irradiance, with calculated and observed data; (c) Photometer B at 530.3 nm normalized to noon irradiance, with calculated and observed data.

the solar disk center at the upper atmosphere with $P(\lambda, t) = \frac{R_{c0}(\lambda, t)}{R_{s0}(\lambda, t)}$, which satisfies

$$P(\lambda, t) = \frac{D_c(\lambda, t)}{R_{\rm sp}(\lambda, t)} \cdot \frac{1}{\tau_c(t)} \cdot k_0. \quad (6)$$

The k_0 characterizes the response coefficient of SICG to the brightness of the solar disk center. Once the photometric calibration coefficient k_0 is determined, the real-time photometric calibration of SICG can be achieved based on the measuring value with the photometer and the count values obtained from coronal observations. Following the processing workflow of Section 2.3, the photometric calibration coefficients k_0 are identified to be 5.01821×10^{-9} at 637.4 nm wavelength and 6.49958×10^{-8} at 530.3 nm wavelength. However, when updating the flat-field calibration using flat-field data from the observational FOV between $1.05R_\odot$ and $2R_\odot$ under the conventional observation mode, the response ratio $\gamma_{\rm rio}$ between the observed region and the solar center must be taken into account. This ratio is determined from the full-field image taken with the internal occulter removed, as shown in Figure 5(c). Specifically, $\gamma_{\rm rio}$ is calculated as the ratio of the maximum flat-field intensity within the observed FOV to the average intensity within a 10 pixel radius around the solar disk center. According to the optical principles and considering the high level of cleanliness maintenance of SICG, the ratio $\gamma_{\rm rio}$ remains constant over a relatively long period. This is further expressed in Equation (7) as

$$P(\lambda, t) = \frac{D_c(\lambda, t)}{R_{\rm sp}(\lambda, t)} \cdot \frac{1}{\tau_c(t)} \cdot k_0 \cdot \frac{1}{\gamma_{\rm rio}}, \quad (7)$$

where $\gamma_{\rm rio} = 0.91$.

3. Validation of Photometric Calibration of SICG

The comparative analysis is crucial and challenging for determining the uncertainty of SICG photometric calibration since it lacks E-coronal brightness data at the same observation wavelength and observing site. Considering that both the coronal structure and atmospheric transparency vary with time, the validation of SICG solar photometer could be fulfilled with the multi-source data as follows.

3.1. Testing of Photometer Measurement

According to the Beer–Bouguer–Lambert law, the spectral irradiance of sunlight decreases exponentially with optical thickness, accounting for the effects of aerosol absorption and scattering (Abitan et al. 2008). By modeling, the coupled aerosol wavelength index and atmospheric turbidity coefficient, defined as α and β separately, are critical parameters for estimating the maximum solar irradiance received on the ground (Khalil & Shaffie 2016). With $\alpha = 3$ and $\beta = 0.01$, the normalized irradiance relative to noon at two wavelengths of 637.4 and 530.3 nm can be calculated throughout the day (2024 February 13) at the SICG observatory site (longitude: 100°2′E, latitude: 26°42′N). The value $\alpha = 3$ corresponds to aerosol particle radii in the range of 0.062–0.1 μm, which is consistent with Rayleigh scattering conditions (Thekaekara 1974). The choice of $\beta = 0.01$ represents an idealized clean atmosphere (Li et al. 2013). As shown in Figure 6(a), the normalized irradiance tends to increase with solar elevation angles, as the total optical thickness decreases, reaching a maximum value of 1 at noon. Obviously, the irradiance variation ratio is slightly larger at 530.3 nm than at 637.4 nm. Meanwhile, the coupled aerosol wavelength index and local altitude significantly affect the maximum value of received solar irradiance on the ground.

For testing, photometers A and B record the solar irradiance intensity at two wavelengths, as shown in Figures 6(b) and (c), where the results are normalized relative to noon on the same day. The overall trend of the two irradiance observations closely aligns with the calculated results, except for discrepancies arising from sporadic thick cloud cover and

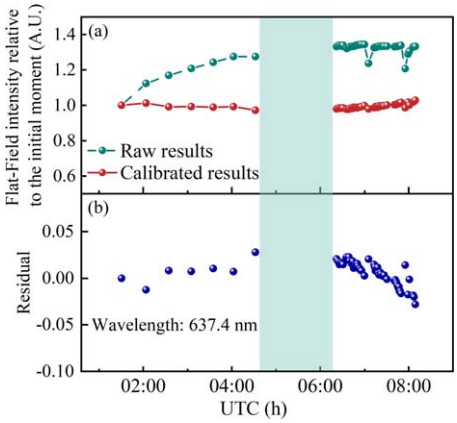

Figure 7. (a) Normalized and compensated results of flat-field total intensity data at 637.4 nm; (b) Relative deviation between the calibrated and the expected results at 637.4 nm. The disturbances caused by sporadic clouds during observation are processed as blocked and marked in green.

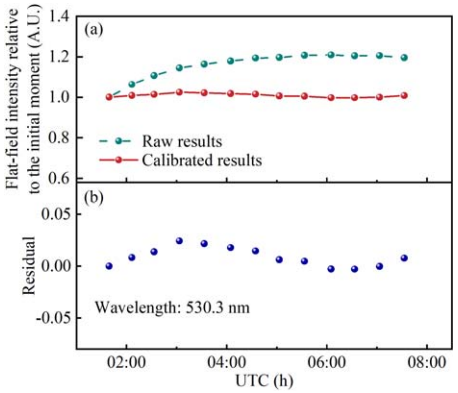

Figure 8. (a) Normalized and compensated results of flat-field total intensity data at 530.3 nm; (b) Relative deviation between the calibrated and the expected results at 530.3 nm.

atmospheric disturbances at times. Especially, the consistency of the measured irradiance trend is better in the afternoon than in the forenoon, which may be attributed to changes in meteorological conditions at the local observing site. At both observational wavelengths, the actual normalized irradiance responds similarly to sky disturbances, confirming the reliability of the solar photometer.

3.2. Flat-field Data Compensation

Considering that flat-field observation is executed with the opal covering the input aperture of SICG and diffusing the photospheric light, this can also serve as a reference for coronal brightness assignment through equivalent substitution. It is generally reasonable that the solar photosphere is the main source of illumination for the opal. Thus, the captured flat-field image reflects both the local solar disk brightness and the flat-field response of the optical system. The former is determined by the solar disk brightness in the upper atmosphere and atmospheric transmittance. As scheduled in Figure 5(c), if the flat-field images are continuously recorded throughout the day, the pixel flux would vary with the atmospheric transmittance alone for the solar photospheric brightness, and the flat-field response of the optical system remains constant. Thus, by employing the photometers, we could simultaneously compensate for the flat-field data, which is similar to coronal photometric correction, with the accuracy being estimated.

At the start of the observation, all pixel DN values of the flat-field image are summed to obtain the total flux, while the photometers record the solar disk intensity. This initial value of flat-field total intensity works as the normalization reference for the next observation moment. Therefore, after compensation with the photometer data, the relative intensity variation of the flat-field data chain is expected to reach the theoretical value of 1. Figures 7 and 8 illustrate the normalized and compensated flat-field total intensity at the wavelengths of 637.4 nm (on 2024 February 13) and 530.3 nm (on 2024 February 13). The results indicate that the raw flat-field total intensity exhibits variations of approximately 34.41% at 637.4 nm and 20.91% at 530.3 nm over the observation duration from 01:30 to 08:00 UTC. This implies that the absorption of the atmosphere along the sunlight propagation path is wavelength-dependent. In order to compensate for these variations using photometer data, the linear relationship between the flat-field total intensity $F(t)$ and the solar flux $f(t)$ was established. Figures 9(a) and (b) show the linear relationship between $F(t)$ and $f(t)$, where the discrete points represent the observed data, and the straight lines indicate the results of the linear regression analysis. The flat-field data, acquired twice daily between 2024 January 15 and February 13, were used for analysis. Outliers caused by atmospheric disturbances (e.g., thick clouds) were excluded based on photometer recordings. Analysis shows that the expressions are $F(t) = 2.96412 \times 10^9 \cdot f_A(t) + 1.4691 \cdot 10^9$ and $F(t) = 2.21385 \times 10^8 \cdot f_B(t) + 8.10129 \cdot 10^8$ separately at wavelength 637.4 and 530.3 nm. Then the corrected total intensity, as given in Figures 7(a) and 8(a), is calculated using observed data from photometers $f_A(t)$ and $f_B(t)$. These data reflect the atmospheric transmission changes with solar elevation angle and time. Additionally, the disturbances caused by sporadic clouds during observation are marked as blocked in Figure 7. In practice, minor fluctuations around the expected value of 1 are observed, primarily due to transient atmospheric disturbances. However, the corrected values at both wavelengths show that their relative deviations from the expected value of 1 are all within $\pm 3\%$, as shown in Figures 7(b) and 8(b). This confirms that the photometric compensation uncertainty for the flat-field data at two wavelengths of 637.4 and 530.3 nm is within $\pm 3\%$, allowing it to be compared with the coronal photometric assignment.

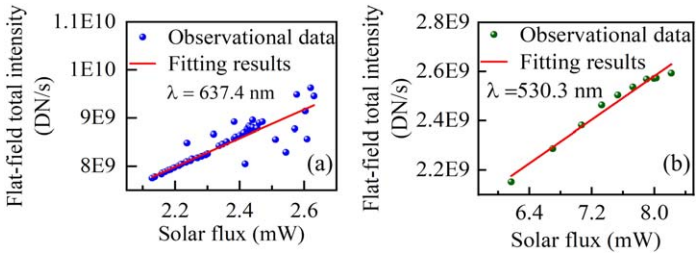

Figure 9. (a) The correspondence between solar flux and flat-field total intensity at 637.4 nm; (b) The correspondence between solar flux and flat-field total intensity at 530.3 nm.

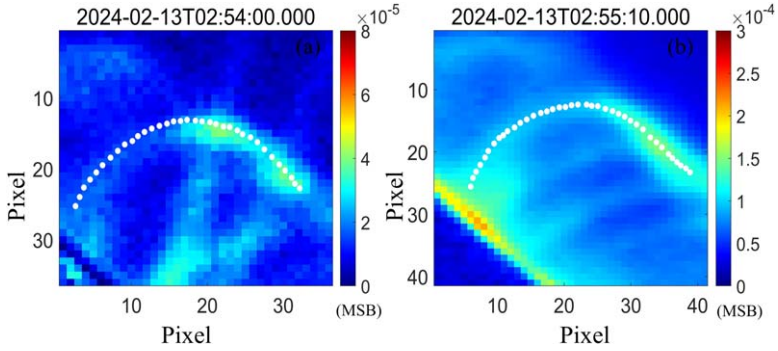

Figure 10. (a) Brightness of coronal loop at 637.4 nm; (b) Brightness of coronal loop at 530.3 nm in the same region.

3.3. Comparison of E-coronal Brightness

Combining the flat-field total intensity $F(t_1)$, the photometers recorded solar flux $f_A(t_1)$ and $f_B(t_1)$ at moment t_1 and $f_A(t)$ and $f_B(t)$ at moment t during observation, the SICG observation data can be corrected by two means for comparison. By substituting the measured flat-field data for the solar disk irradiance value in Equation (6), it is equivalently transformed into

$$\begin{cases} P(\lambda, t) = \frac{D_c(\lambda, t)}{F_{\text{cal}}(t)} \cdot \text{fac} \\ F_{\text{cal}}(t) = \frac{k \cdot f(t) + b}{k \cdot f(t_1) + b} \cdot F(t_1), \\ \text{fac} = \frac{F(t_0)}{D_s(\lambda, t_0)} \end{cases} \tag{8}$$

where $F_{\text{cal}}(t)$ represents the flat-field observation data following photometric compensation, derived from the process flow in Section 3.2. The calibration factor, fac, for flat-field photometric assignment is achieved from flat-field and solar disk observation data, with CCD camera dark-field subtraction and normalization to unit exposure time. The final calibration factor, fac, is 13.866×10^{-6} (MSB) at 637.4 nm and 12.1381×10^{-6} (MSB) at 530.3 nm. Extracting the E-coronal observation data $D_c(\lambda, t)$ according to the data processing workflow in Figure 4 allows for the determination of E-coronal brightness using Equation (8).

Figures 10(a) and (b) show the partial views of SICG images, where a multi-temperature coronal loop is observed at 637.4 and 530.3 nm at 02:54:00 UTC. The distributions of E-coronal brightness along the loop, corrected with the flat-field total intensity and the photometer solar flux, are illustrated in Figures 11(a) and (b) at 637.4 nm and 530.3 nm, respectively. Furthermore, the deviations of the two processed brightness values are computed with relative deviations of 2.1% and 2.3% for 637.4 and 530.3 nm. Figure 12 reveals the relative deviation in E-coronal brightness, accounting for coronal loop evolution and atmospheric transmittance variations with time. Throughout the observation period, the calibration deviation remains below 2.1% at 637.4 nm and about 2.3% at 530.3 nm. Although potential systematic errors may influence the results, this calibration methodology demonstrates relatively low uncertainty under typical coronal observing conditions. However, the technique is limited by intermittent thick cloud cover, during which photometric measurements approach instrumental noise floor levels. Since such atmospheric conditions compromise coronal observations, affected data points need to be excluded as outliers during photometric calibration. Additionally, while this calibration scheme effectively characterizes coronal brightness, its current implementation does not directly improve the measurement precision of Doppler velocity or spectral line width. Future methodological developments will focus on extending the calibration framework to incorporate these additional diagnostic parameters.

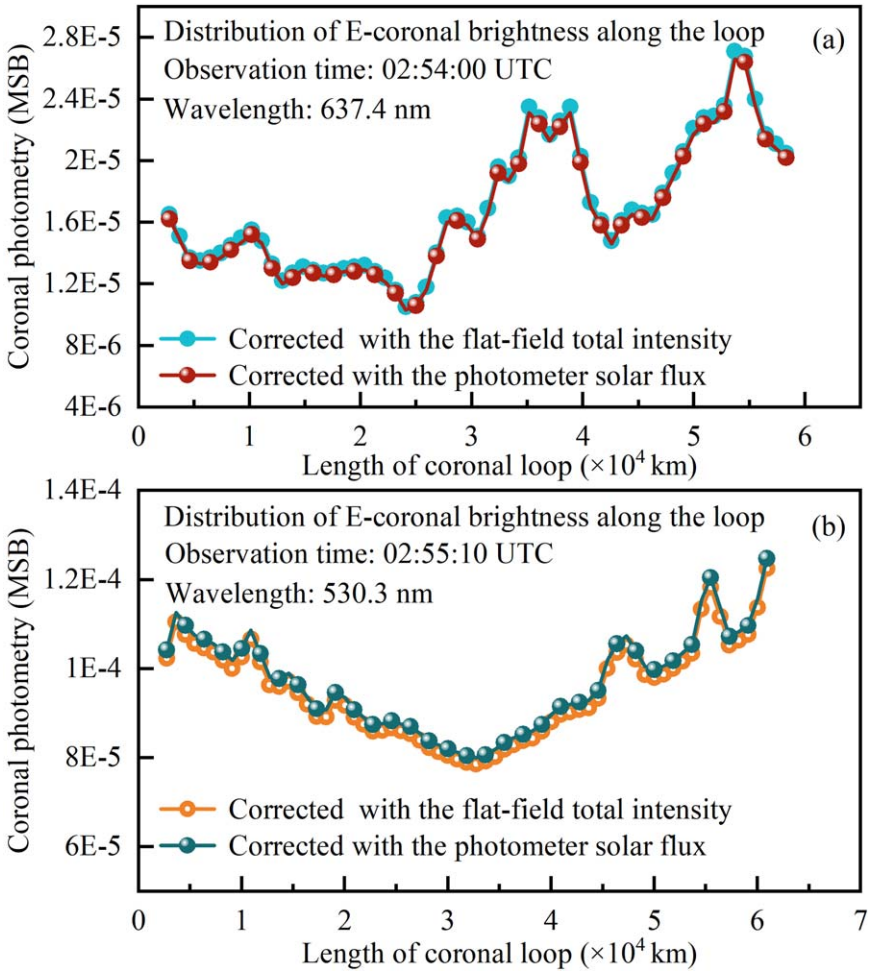

Figure 11. (a) E-coronal brightness at 637.4 nm. The blue line represents the brightness corrected with the flat-field total intensity, while the red line represents the brightness corrected with photometer solar flux; (b) E-coronal brightness at 530.3 nm. The green line represents the brightness corrected with the flat-field total intensity, while the orange line represents the brightness corrected with the photometer solar flux.

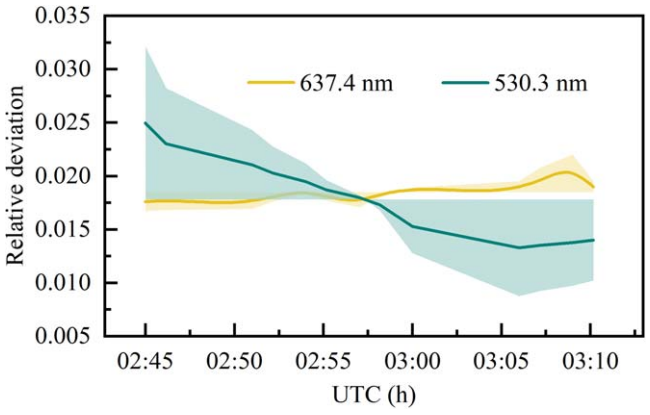

Figure 12. Relative deviation in E-coronal brightness with two processing methods. The shaded regions reflect the deviation of each data point relative to the average value, representing the variability of the relative deviation.

4. Analysis of E-coronal Evolution Based on Brightness Data

The photometric calibration of SICG is very crucial in many research subjects, such as exploring the temporal evolution of E-coronal loops. Following the processing workflow in Figure 4, the coronagraph data at two wavelengths are calibrated and compared. Figure 13 presents the time-slice plot of E-coronal brightness along the coronal loop shown in Figure 10 at 637.4 nm (Fe X line) and 530.3 nm (Fe XIV line) over an 11 minutes period from 02:43 to 02:54 UTC on 2024 February 13. In Figure 13(a), the blue crosses indicate the positions of the maximum brightness along the coronal loop at each observation moment, connected by green lines. It shows an obvious brightening at the apex of the loop, with the brightened plasma propagating toward the footpoints along the loop at a velocity of $\pm 30\,\mathrm{km\,s^{-1}}$, as calculated by linear

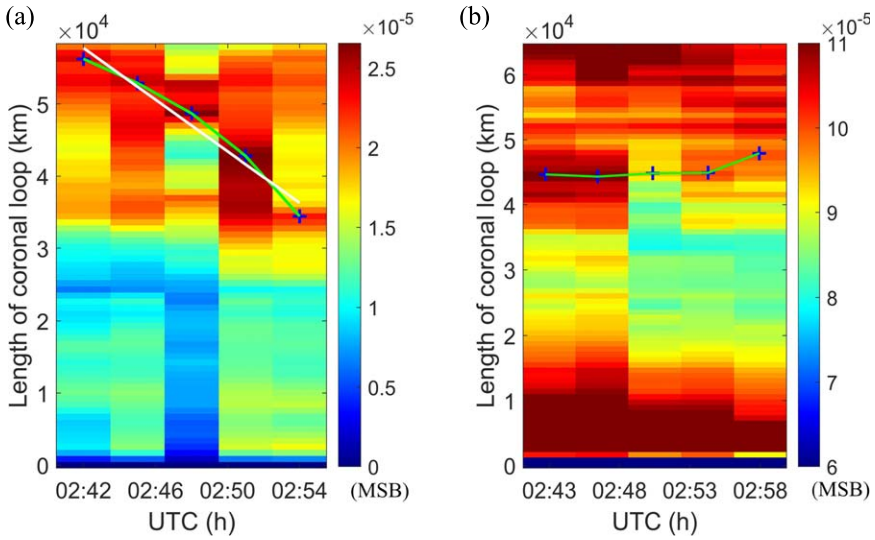

Figure 13. (a) Time-slice plot of E-coronal at 637.4 nm (Fe X line); (b) Time-slice plot of E-coronal at 530.3 nm (Fe XIV line). The blue crosses indicate the positions of the maximum brightness along the coronal loop at each observation moment. The green sectors represent the connecting lines of the blue crosses, which are used for linear regression analysis (white lines) to determine the propagation speed.

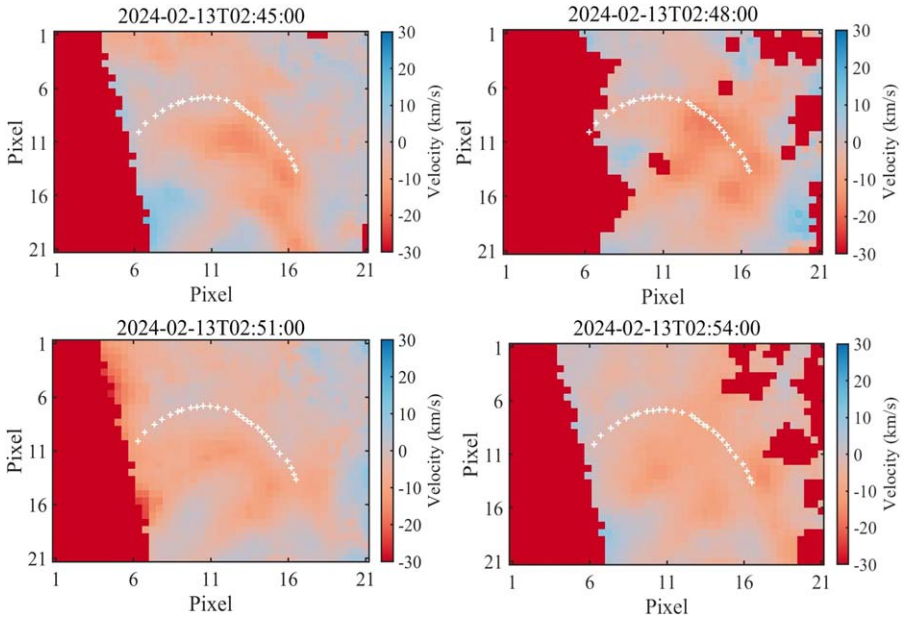

Figure 14. Doppler velocity map at 637.4 nm.

regression analysis (white lines). Given that Doppler velocity data have been proven to be a powerful tool for diagnosing CME properties, coronal wave dynamics, and coronal magnetic fields (Tomczyk et al. 2007; Tian et al. 2013; Yang et al. 2024), Figure 14 shows the Doppler velocity distribution corresponding to the observation period. The loop shown in Figure 10(a) is marked with white crosses in Figure 14, where a distinct redshift is clearly observed. This provides direct evidence of propagation behavior, indicating plasmoid motion along the loop. Additionally, Figure 13(b) indicates that the coronal loop at 530.3 nm remains relatively stable. Although the entire loop appears bright, the photometric values are relatively uniform. Considering that the coronal structure at 530.3 nm refers to Fe XIV line with a formation temperature around 2 MK and that at 637.4 nm corresponds to Fe X line at around 1 MK, the multi-temperature analysis suggests that in

this coronal loop, the plasmoid with a temperature of 1 MK or higher but below 2 MK exhibits clear propagation behavior. Also, the coronal loop exhibits higher density at the two ends as to the plasma at 2 MK, while the density almost monotonically changes as to the plasma at 1 MK. Since the plasma material transports downward with a speed of approximately $\pm 30\ \mathrm{km\ s^{-1}}$ as shown in Figure 13(a), a possible explanation is that the thermal structure of plasma at 1 MK is more non-uniform than that at 2 MK and would be dominated by magnetic fields or thermal gravity.

The calibrated photometric data of SICG enable the quantitative analysis of coronal loop evolution and allow the comparative investigation of the physical formation mechanisms of multi-temperature structures. However, the current observational data cannot provide magnetic field information directly. To further explore the driving mechanisms of coronal loop evolution, it is necessary to combine the SICG data with high-resolution observations from AIA and magnetic field data from HMI.

5. Conclusions

This paper proposes a method for calibrating the photometry of the dual-wavelength SICG using two self-developed photometers, thereby establishing the photometric calibration method and data processing workflow for the coronagraph. Based on this methodology, photometric calibration coefficients for the working wavelengths of 637.4 and 530.3 nm are provided. The comparison between the model analysis and flat-field observation data demonstrates that the calibration results meet the requirements for scientific research. Building on these results, the evolutionary speed of multi-temperature coronal loops was tracked and analyzed. Furthermore, by integrating magnetic field data, this research will contribute to a deeper study of the physical evolution mechanisms.

Acknowledgments

This work is supported by the Chinese Meridian Project (CMP) and the National Natural Science Foundation of China (grant Nos. 42230203, 42374220, and 12173086).

References

Abitan, H., Bohr, H., & Buchhave, P. 2008, ApOpt, 47, 5354
Aschwanden, M. J., & Nitta, N. 2000, ApJL, 535, L59
Brueckner, G., Howard, R., Koomen, M., et al. 1995, SoPh, 162, 357
Casini, C., Da Deppo, V., Zuppella, P., et al. 2021, Proc. SPIE, 11852, 118525B
Colaninno, R., & Howard, R. 2015, SoPh, 290, 997
de Wijn, A. G., Burkepile, J. T., Tomczyk, S., et al. 2012, Proc. SPIE, 8444, 84443N
Fineschi, S., Antonucci, E., Naletto, G., et al. 2012, Proc. SPIE, 8443, 84433H
Howard, R. A., Moses, J., Vourlidas, A., et al. 2008, SSRv, 136, 67
Judge, P., Berkey, B., Boll, A., et al. 2019, SoPh, 294, 1
Kaiser, M. L., Kucera, T., Davila, J., et al. 2008, SSRv, 136, 5
Khalil, S. A., & Shaffie, A. 2016, RSERv, 54, 363
Kohl, J. L., Jain, R., Cranmer, S. R., et al. 2008, JApA, 29, 321
Li, J.-Y., Zhan, J., Xu, Q.-S., & Wei, H.-L. 2013, AstTI, 10, 185
Liu, D.-Y., Yu, X.-Y., Zhang, H.-X., et al. 2025, RAA, 25, 015014
Ltaief, H., Cranney, J., Gratadour, D., et al. 2021, in SC '21: The International Conf. for High Performance Computing, Networking, Storage (New York: Association for Computing Machinery), 1
Marois, C., Lafreniere, D., Macintosh, B., & Doyon, R. 2006, ApJ, 647, 612
Minarovjech, M., Rušin, V., Rybanský, M., Sakurai, T., & Ichimoto, K. 2003, SoPh, 213, 269
Morrill, J., Korendyke, C., Brueckner, G., et al. 2006, SoPh, 233, 331
Morton, R., Tomczyk, S., & Pinto, R. 2016, ApJ, 828, 89
Newmark, J., Cook, J., & Moses, J. 2007, Proc. SPIE, 6689, 668902
Ouyang, C., Plonus, M., & Wang, S. 1981, ApOpt, 20, 786
Raouafi, N. E., Matteini, L., Squire, J., et al. 2023, SSRv, 219, 8
Sha, F., Liu, Y., Zhang, X., & Song, T. 2023, SoPh, 298, 139
Sivaramakrishnan, A., & Oppenheimer, B. R. 2006, ApJ, 647, 620
Tang, N., Yu, X., Liu, D., et al. 2023, ChJG, 66, 881
Thekaekara, M. P. 1974, ApOpt, 13, 518
Tian, H., Tomczyk, S., McIntosh, S., et al. 2013, SoPh, 288, 637
Tomczyk, S., Card, G., Darnell, T., et al. 2008, SoPh, 247, 411
Tomczyk, S., McIntosh, S., Keil, S., et al. 2007, Sci, 317, 1192
Wang, C., Chen, Z., & Xu, J. 2020, ChJSS, 40, 718
Xin, Y.-X., Bai, J.-M., Lun, B.-L., et al. 2020, RAA, 20, 149
Yang, Z., Tian, H., Tomczyk, S., et al. 2024, Sci, 386, 76
Zaki, W., Zidane, A., & Al-Sawad, A. 2016, IJAA, 6, 276
Zhang, X.-F., Liu, Y., Zhao, M.-Y., et al. 2022, RAA, 22, 075007